

## Partial volume effect correction in PET using regularized iterative deconvolution with variance control based on local topology

A S Kirov<sup>1</sup>, J Z Piao<sup>2</sup> and C R Schmidlein<sup>1</sup>

<sup>1</sup> Memorial Sloan-Kettering Cancer Center, New York, NY 11021, USA

<sup>2</sup> The Cleveland Clinic, Cleveland, OH 44195, USA

E-mail: [kirova@mskcc.org](mailto:kirova@mskcc.org)

Received 4 October 2007, in final form 21 March 2008

Published 25 April 2008

Online at [stacks.iop.org/PMB/53/2577](http://stacks.iop.org/PMB/53/2577)

### Abstract

Correcting positron emission tomography (PET) images for the partial volume effect (PVE) due to the limited resolution of PET has been a long-standing challenge. Various approaches including incorporation of the system response function in the reconstruction have been previously tested. We present a post-reconstruction PVE correction based on iterative deconvolution using a 3D maximum likelihood expectation-maximization (MLEM) algorithm. To achieve convergence we used a one step late (OSL) regularization procedure based on the assumption of local monotonic behavior of the PET signal following Alenius *et al.* This technique was further modified to selectively control variance depending on the local topology of the PET image. No prior ‘anatomic’ information is needed in this approach. An estimate of the noise properties of the image is used instead. The procedure was tested for symmetric and isotropic deconvolution functions with Gaussian shape and full width at half-maximum (FWHM) ranging from 6.31 mm to infinity. The method was applied to simulated and experimental scans of the NEMA NU 2 image quality phantom with the GE Discovery LS PET/CT scanner. The phantom contained uniform activity spheres with diameters ranging from 1 cm to 3.7 cm within uniform background. The optimal sphere activity to variance ratio was obtained when the deconvolution function was replaced by a step function few voxels wide. In this case, the deconvolution method converged in  $\sim 3$ –5 iterations for most points on both the simulated and experimental images. For the 1 cm diameter sphere, the contrast recovery improved from 12% to 36% in the simulated and from 21% to 55% in the experimental data. Recovery coefficients between 80% and 120% were obtained for all larger spheres, except for the 13 mm diameter sphere in the simulated scan (68%). No increase in variance was observed except for a few voxels neighboring strong activity gradients and inside the largest spheres. Testing the method for patient images increased the visibility of small lesions in non-uniform background and preserved the overall

image quality. Regularized iterative deconvolution with variance control based on the local properties of the PET image and on estimated image noise is a promising approach for partial volume effect corrections in PET.

(Some figures in this article are in colour only in the electronic version)

## 1. Introduction

Finite scanner resolution prevents quantification for objects with size comparable and smaller than about two to three times the full width at half-maximum (FWHM) of the scanner's point spread function (PSF). This loss of quantitative accuracy for hot and cold spot contrast recovery is an effect known as the partial volume effect (PVE) (Hoffman *et al* 1979, 1982, Kessler *et al* 1984). The finite PET scanner resolution is due to the positron range prior to annihilation, positronium residual momentum at annihilation, which causes annihilation photon non-colinearity, finite crystal size, inter-crystal scatter, depth of penetration uncertainty and artifacts introduced by the re-binning and reconstruction algorithms (Phelps *et al* 1975, Levin and Hoffman 1999, Sanchez-Crespo *et al* 2004, Tomic *et al* 2005, Alessio *et al* 2006).

Various approaches for correcting the PVE have been previously tested. One possible classification of these methods was recently published (Soret *et al* 2007). It divides them into two large groups depending on whether the correction was applied at regional level targeting improved quantification for a selected region or on a voxel level, targeting resolution correction of entire images. On the other hand the methods, which specifically use the PET system response, can also be divided into two broad categories.

The first category includes methods, which account, and thereby correct, for the point spread function during the reconstruction. Earlier works in this direction include combining a Fourier transform of the positron range distribution function with the Fourier transform of the reconstruction filter in filtered back-projection (FBP) reconstruction (Haber *et al* 1990). The penalized maximum likelihood algorithm has been used to correct the projections from the sinogram for a modeled detector response before filtering in the filtered back-projection algorithm (Liang 1994). PSF deconvolution of re-binned 3D data prior to 2D reconstructions has also been performed (Alessio *et al* 2006). One of the recent and most comprehensive methods incorporates an accurate model of the overall spatially variant PET system response in the projection matrix of a statistical reconstruction algorithm (Alessio and Kinahan 2006). In an even more recent paper, deconvolution was performed prior to each subsequent iteration during ordered sub-sets expectation maximization (OSEM) reconstruction (Rizzo *et al* 2007).

The second category includes methods, which apply a resolution correction to the PET images post-reconstruction. Most of these methods calculate in one way or another the PET signal spill-over from one structure to another and then attempt to correct for it (Rousset *et al* 1998). Such methods either use prior anatomic information to define the volumes of elevated activity and to control variance within the rest of the image (Boussion *et al* 2006, Turkheimer *et al* 2008) or do not address the increase in variance (Teo *et al* 2007). However, the assumption that the regions with elevated PET tracer concentration (TC) conform to the anatomical structures is not correct for oncologic studies, where the metabolically active tumor often may not fill an entire organ as defined by computer tomography (CT) or magnetic resonance imaging (MRI) or may protrude in the neighboring tissues.

Therefore, such methods are vulnerable to some degree to one of the following disadvantages, which decrease their potential for clinical use: (i) unacceptable increase of variance in the image; (ii) bias due to image registration or biology/metabolism-based mismatch between TC and the anatomical information from CT or MRI.

In this paper, we present a PVE correction method that is based upon post-reconstruction iterative deconvolution. We tested deconvolution functions with shapes different from the scanner's point spread function. In order to avoid an increase in variance, we applied and modified the one step late (OSL) regularization procedure (Alenius and Ruotsalainen 1997). It was modified to impose variable penalty based on the local topology of the PET signal, avoiding in this way any dependence upon tracer uptake conformity with anatomical information. The method was tested on simulated and real PET phantom scans.

While this paper was in review, a conference report (Boussion *et al* 2007), describing a PVE correction method operating at the voxel level, which also does not depend on anatomical information and is based on a different, fully automatic, wavelet-based de-noising approach, appeared.

## 2. Methods and materials

### 2.1. Deconvolution algorithm

The iterative three-dimensional deconvolution program is obtained by replacing the projection kernel in a MLEM algorithm for SPECT (Wallis and Miller 1993) by a user-defined point spread function (Kirov *et al* 2005). The tracer concentration (TC) estimated from the PET scan,  $C_a$ , is a result of a 3D convolution:

$$C_a(\vec{u}) = P(\vec{u}|\vec{r}) \otimes C_b(\vec{r}), \quad (1)$$

where  $\vec{r}$  and  $\vec{u}$  are the three-dimensional coordinates in the measurement space,  $P(\vec{u}|\vec{r})$  is the point spread function (PSF) value for the displacement vector,  $\vec{r} - \vec{u}$ , and  $C_b(\vec{r})$  is the true TC distribution to be retrieved. The non-negativity of the TC and the point spread function allows us to use Csiszar's I-divergence (Csiszar 1991) as a discrepancy measure within MLEM (Snyder *et al* 1992). The estimate of the true TC,  $\hat{C}_b(\vec{r})$ , after  $k+1$  iterations is then given by

$$\hat{C}_b^{k+1}(\vec{r}) = \hat{C}_b^k(\vec{r}) \frac{1}{\sum_{\vec{u} \in A(\vec{r}, R_{\text{PSF}})} P(\vec{u}|\vec{r})} \sum_{\vec{u} \in A(\vec{r}, R_{\text{PSF}})} \left[ \frac{C_a(\vec{u})}{\sum_{\vec{r}' \in B(\vec{u}, R_{\text{PSF}})} P(\vec{u}|\vec{r}') \hat{C}_b^k(\vec{r}')} \right] P(\vec{u}|\vec{r}), \quad (2)$$

where  $\hat{C}_b^k(\vec{r}')$  is the TC distribution estimate after  $k$  iterations. By comparing the terms in (2) to those in (1), one can see that the next estimate of the TC in each voxel is obtained by multiplying the current estimate by the sum of the inaccuracy ratios for each of the neighboring voxels from the current estimate weighted by the corresponding PSF values  $P(\vec{u}|\vec{r})$ . A measure,  $\varepsilon(\vec{u})$ , of the inaccuracy of the  $k$ th estimate at voxel  $\vec{u}$  can be expressed using the term in (2) representing this ratio:

$$\varepsilon(\vec{u}) = \left[ \frac{C_a(\vec{u})}{\sum_{\vec{r}' \in B(\vec{u}, R_{\text{PSF}})} P(\vec{u}|\vec{r}') \hat{C}_b^k(\vec{r}')} \right] - 1. \quad (2a)$$

The effect of the PSF to each voxel  $\vec{u}$  is limited to a cubic region with side  $2R_{\text{psf}} + 1$  voxels centered at  $\vec{u}$ , where  $R_{\text{psf}}$  is a user-defined parameter.

Since the direct implementation of (2) results in a limited contrast recovery accompanied with a strong variance increase (Snyder *et al* 1987), in this paper we depart from the common assumption that the PSF,  $P(\vec{u}|\vec{r})$ , needs to match the scanner point spread function, which is often approximated by a Gaussian-type function. In fact, we suggest using a function that is

more slowly varying than the scanner PSF. From now on we will refer to it as the deconvolution function (DF). We expect that using such a slowly varying DF will

- (1) limit the variance increase throughout the image by calculating the inaccuracy ratios  $1 + \varepsilon(\vec{u})$  in (2) with respect to the activity closer to the mean activity of the region  $B(\vec{u}, R_{\text{PSF}})$  around the voxel, rather than with respect to the activity estimate for voxel  $\vec{u}$ , which it represents when the scanner PSF is used,
- (2) reduce variance in the uniform activity regions by more equally weighted averaging of the inaccuracy ratios  $1 + \varepsilon(\vec{u})$  of the previous ( $k$ )th activity estimate within the region around each voxel (a Gaussian-shaped PSF will give larger weight to the inaccuracies closer to the center of the Gaussian, which may be noisier) and
- (3) enhance the deconvolution for the regions that have stronger activity variation (i.e. tumor edges), where the inaccuracy measure  $1 + \varepsilon(\vec{u})$  is expected to have both larger values and variation.

This modification of the deconvolution procedure has a strong theoretical background. In general any deconvolution of noisy data is an attempt to solve an ill-posed mathematical problem if the solution is being searched among all possible functions. In the case of PET that would be all mathematically possible activity distributions (Fedorenko 1994). Real activity distributions are expected to be smoother than PET images with limited statistics, which are noisy. Therefore, the correctness can be improved if the solution is limited to a narrower space of smoother functions. This is what, we expect, the substitution of the scanner PSF with a more slowly varying function will accomplish: using a more uniform, i.e. broader width, PSF will effectively impose stronger smoothness on the solution and thereby improve the correctness of the problem. In this way, it is introducing additional regularization to the one step late regularization described in section 2.2.

To show this, we varied the point spread function's FWHM. We tested the Gaussian shape DFs with FWHM of 6.31 mm, 18.93 mm ( $= 6.31 \times 3$ ), 31.55 mm ( $= 6.31 \times 5$ ) and an infinite value (i.e. a step function).

To enhance convergence, a median root prior (MRP) filter (Alenius and Ruotsalainen 1997) is implemented (Piao and Kirov 2001, Kirov *et al* 2005) using a one step late (OSL) MRP algorithm:

$$\hat{C}_b^{k+1}(\vec{r}) = \frac{\hat{C}_b^{k+1,\text{dec}}(\vec{r})}{1 + \beta \frac{\hat{C}_b^k(\vec{r}) - M_R}{M_R}}. \quad (3)$$

Here,  $\hat{C}_b^{(k+1),\text{dec}}(\vec{r})$  is the  $(k + 1)$ th estimate of the emission density in voxel at position  $\vec{r}$  after the PSF deconvolution (1) but before MRP regularization,  $\hat{C}_b^{(k)}(\vec{r})$  and  $\hat{C}_b^{(k+1)}(\vec{r})$ , respectively, are the  $k$ th and  $(k + 1)$ th estimates of the emission density at position  $\vec{r}$  after the MRP regularization,  $M_R = \text{Med}(\hat{C}_b^k, \vec{r}, R)$  is the median voxel value in a small neighborhood with radius  $R$ , around the voxel at  $\vec{r}$ , and  $\beta$  is the weight of the prior.

## 2.2. Topology adaptive regularization

The regularization parameters in (3) are the weight  $\beta$  and the radius of the neighborhood  $R$  for calculating  $M_R$ . In order to restrict the variance increase in the images we varied the weight  $\beta$ , so that stronger regularization is applied to background parts of the image. Regions close to the image edges were also assigned stronger regularization ( $\beta_1$ ) to suppress the known edge artifacts of the ML algorithm. Regions with activity variations larger than the background noise, which could reveal potential lesions, were assigned weaker regularization ( $\beta_2$ ).

To do this we select two more neighborhoods around each point in which to check the minimum activity and the variation of activity against fractions ( $k_1$  and  $k_2$ ) of the background value. These two neighborhoods would generally have different radii ( $R_1$  and  $R_2$ ), smaller than  $R$ , in order to preserve the gradients in these regions of the image.

For a neighborhood with radius  $R_1$  around each voxel, we find the minimum activity voxel,  $P_{\min,R_1}$ , and for a neighborhood with radius  $R_2$  we find the minimum,  $P_{\min,R_2}$ , and the maximum,  $P_{\max,R_2}$ , voxel values. Let  $M_{\text{bkg}}$  be a rough estimate of the entire image's background level (note that  $M_{\text{bkg}}$  is not the same as  $M_R$  used above and can be visually determined by observing activity profiles through the images). Then the PET image data set can be effectively divided into three parts: regions of interest in which the activity undergoes a change above a certain threshold (regularized with weight  $\beta_2$ ), background regions (regularized with  $\beta_0$ ) and regions around the image edges (regularized with  $\beta_1$ ) following these conditions:

$$\beta = \left\{ \begin{array}{ll} \beta_0 & \text{elsewhere} \\ \beta_1 & \text{for } P_{\min,R_1} < k_1 \cdot M_{\text{bkg}} \\ \beta_2 & |P_{\max,R_2} - P_{\min,R_2}| > k_2 \cdot M_{\text{bkg}} \end{array} \right\}, \quad (4)$$

where  $R_1$ ,  $R_2$ ,  $k_1$ ,  $k_2$  and  $M_{\text{bkg}}$  as well as  $\beta_0$ ,  $\beta_1$  and  $\beta_2$  are parameters set by the user.

While these parameters seem many, they do represent a clear example of how one can intuitively adapt the strength of the regularization to the image topology. In fact these parameters represent an efficient approach to assign an appropriate value for the regularization weight,  $\beta$ , in different parts of the image. As shown in section 3.1.2 they turned to have stable values for the tested images.

The algorithm proceeds as follows. A weight value  $\beta = \beta_0$  is initially assigned for the entire data set for each PET scan. This value is relatively high ( $\sim 0.9$ ) and is set to control variance in the background portions of the images, where the increase of variance due to the deconvolution needs to be suppressed most.

Next, a check corresponding to the second line of (4) may change  $\beta$  if it is close to the regions with PET signal significantly lower than the average image background ( $k_1 \sim 0.3$ ), i.e. around air cavities or outside the patient. This check imposes an even higher regularization weight ( $\beta \sim 1$ ), which is necessary to penalize the so-called 'edge artifacts' (Snyder *et al* 1987) of the MLEM algorithm. This artifact usually manifests as elevated activity at the surface of the patient's skin.

Finally, a check corresponding to the third line of (4) may reduce  $\beta$  to a lower value,  $\beta_2$ , for regions in which the PET signal fluctuations exceed an empirically determined fraction of the background signal,  $M_{\text{bkg}}$ . These regions would correspond to noticeable activity changes for which the weaker penalty allows stronger deconvolution.

The user selects what fraction,  $k_2$ , of the background activity level would be considered noise. For activity changes larger than  $k_2 \cdot M_{\text{bkg}}$ , the regularization is relaxed since they would be considered significant. For both the simulated and experimental phantom scans, the magnitude of these 'noticeable' activity variations was determined to be close to the magnitude of the background signal ( $k_2 \sim 0.9$ ). In the clinic, this threshold value will be probably determined by a radiologist.

### 2.3. Scanner and phantoms

The deconvolution program was applied to the simulated and real images of the NEMA NU 2 image quality phantom obtained using the GE Discovery LS PET/CT (DLS) scanner.

The *simulated data* were obtained with the GATE (Geant4 Application for Tomographic Emission) Monte Carlo (MC) code for the case of higher ( $14.98 \text{ kBq mL}^{-1}$ ) activity

concentration in the 10, 13, 17 and 22 mm diameter spheres, no activity in the 28 and 37 mm diameter spheres and lower ( $3.98 \text{ kBq mL}^{-1}$ ) activity concentration in the rest of the phantom. We used a previously validated GATE MC model of this scanner in 3D mode (Schmidtlein *et al* 2005, 2006). The data were reconstructed with MLEM using the software for tomographic image reconstruction (STIR). The images contained  $256 \times 256$  voxels with 2.148 44 mm size in the  $x$  and  $y$  directions and 4.25 mm in the  $z$  direction.

The *experimental data* were obtained using 2D high-resolution mode using our clinical settings on a GE Discovery LS PET/CT scanner. In the experiment, all six spheres were filled with an activity concentration of  $21.98 \text{ kBq mL}^{-1}$  and the background activity was  $5.5 \text{ kBq mL}^{-1}$ . The data were collected using a 15 min acquisition and reconstructed with the MLEM algorithm of the scanner. The images contained  $128 \times 128$  voxels with 4.6875 mm size in the  $x$  and  $y$  directions and 3.27 mm in the  $z$  direction.

The mean contrast recovery coefficients (RC) were calculated as outlined in the NEMA NU 2 protocol (NEMA 2001) using circular regions inside the spheres in the central slice and 60 circular regions for the background around them.

The method was also tested for a patient PET scan obtained in our clinic on the Discovery LS PET/CT scanner using  $^{18}\text{F}$ -fluoro-deoxyglucose (FDG) in 2D mode. The images contained  $128 \times 128$  voxels with 3.906 25 mm size in the  $x$  and  $y$  directions and 4.25 mm in the  $z$  direction.

#### 2.4. Deconvolution and regularization parameters

For the deconvolution weighting function we tested a symmetric 3D Gaussian with full width at half-maximum (FWHM) varying from 6.31 mm (the approximate mean PSF of the scanner) to infinity. The radius of this function was varied from 2 to 3 voxels for the experimental scans and from 3 to 6 voxels for the simulated data to reflect the difference in voxel size between the two images.

Alenius (1999) suggested that the radius  $R$  of the monotonicity neighborhoods should be selected to approximate the width of the smallest detail to be preserved. We selected  $R_1$  and  $R_2$  to approximate the width of the high gradient regions at the edges of the image and spheres.

The regularization weights,  $\beta_0$ ,  $\beta_1$  and  $\beta_2$ , were optimized to satisfy the following criteria: (i) to reach convergence; (ii) to obtain recovery coefficients closest to unity for all spheres; (iii) to control the increase of variance in the background regions and the phantom edges and thereby to obtain smoother images with better visible lesions and less artifacts. For monotonicity neighborhoods 3 voxels wide,  $\beta \sim 0.3$  was previously suggested (Alenius 1999) and we tested similar values for the areas of interest in the image containing elevated activity. Values for  $\beta_0$  and  $\beta_1$  closer to 1.0 (Alenius and Ruotsalainen 1997) were experimented for the background and edge regions to suppress variance. Alenius and Ruotsalainen (1997) have shown convergence for this range of values.

The background activity parameter  $M_{\text{bkg}}$  was obtained by a visual estimate of an activity profile observation (figure 2) to approximate the average PET image background level. It is specific for each image and was selected to be 3800 and 5000, which approximate the background activity levels in  $\text{Bq mL}^{-1}$  for the simulated and experimental images, respectively.

The fractions  $k_1$  and  $k_2$  of the background TC,  $M_{\text{bkg}}$ , were selected by observing the image to give TC threshold values of less than a fraction ( $\sim 1/3$ ) of  $M_{\text{bkg}}$ , for  $k_1$ , and exceeding the maximum TC variance ( $\sim 35\%$ ) in the background part of the image, for  $k_2$ . The optimal parameters found are given in table 1.

The PVE correction (we did not need to test more than 14 iterations) takes about 15–20 min for the simulated  $256 \times 256$  pixel images and less than 5 min for the experimental

**Table 1.** Selected deconvolution and regularization parameters used for the simulated (top row) and experimental scans (bottom row).

Deconvolution function		Regularization parameters							
		Image		Edges			Peaks		
FWHM	$R_{DF}$	$R$	$\beta$	$k_1$	$R_1$	$\beta_1$	$k_2$	$R_2$	$\beta_2$
Infinite	4	4	0.9	0.3	3	1.1	0.9	2	0.35
Infinite	3	4	0.9	0.3	3	1.1	0.9	2	0.35

128 × 128 mm images on a 3.2 GHz CPU. The computation time depends upon the deconvolution and regularization parameters used.

### 3. Results

PET images and activity profiles before and after applying the PVE correction are presented in figures 1, 2, 4 and 6. The effects of the FWHM of the deconvolution function on the recovery of peak activity and on the signal to background fluctuations are presented in figure 3. The effect of the PVE correction on the recovery coefficients calculated following the NEMA NU 2 protocol is presented in figure 5.

#### 3.1. Parametric study

**3.1.1. Deconvolution function.** Without regularization (equation (3)) no convergence of the iterative procedure (equation (2)) is observed for any of the different deconvolution functions (DF) used. With regularization and using a Gaussian-shaped DF approximating, the experimental PSF of the scanner (FWHM = 6.31 mm) resulted in insufficient recovery of the activity of the two smallest spheres accompanied by a strong increase of variance, which reached the intensity of the smallest sphere at ~15 iterations. Increasing the width of the DF enhanced the contrast recovery (figures 2(b) and 3). To investigate this we calculated the (peak activity in sphere)/(peak activity in background fluctuations) ratios along the profile shown in figure 2(b). In figure 3 is plotted this ratio divided by the true signal over background ratio of 3.57 (=14.2 kBq mL<sup>-1</sup>/3.98 kBq mL<sup>-1</sup>).

The cut-off radius of the DF was also found to affect the strength of the deconvolution—larger radius leads to stronger deconvolution for both sets of data. Using radii of 4, 5 and 6 voxels for the simulated scan and radii of 2 and 3 voxels for the experimental scan (i.e. cubes with sides 5 and 7 voxels) resulted in similar quality images. Images with optimal contrast recovery and minimum image distortions with identical regularization parameters were observed when radii of 4 and 3 voxels were used for the two data sets, respectively.

**3.1.2. Regularization parameters.** Imposing regularization on the deconvolution process enforced convergence within 3–5 iterations for both the simulated and experimental data and brought the maximum activity in the spheres and the peak sphere to background ratios closer to those of the true values (figure 3). Additional iterations (up to 14) were found to have negligible effect on the result as shown in figure 4. A set of regularization parameters found to work optimally for both data sets is shown in table 1.

Applying an MRP penalty of  $\beta = 0.9$  to the entire image limits the variance increase caused by deconvolution in the parts of the images with small activity changes. Such a

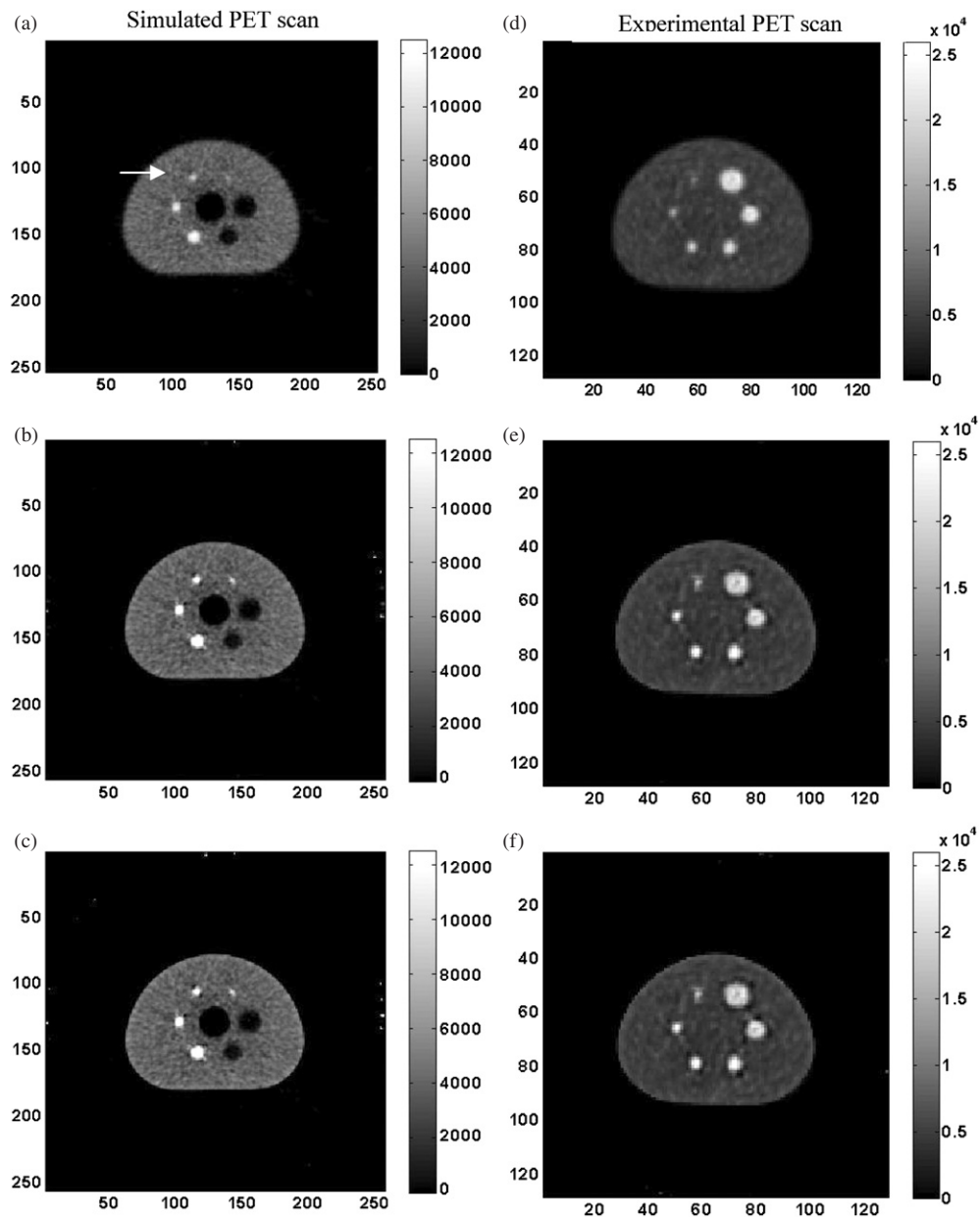


**Figure 1.** PET images (in pixels and in Bq/pixel) of the NEMA NU 2 image quality phantom before (a), (d) and after PSF deconvolution for the simulated (left) and experimental scans (right) with 5 (b), (e) and 15 iterations (c), (f). The arrow in (a) indicates the approximate position of the profiles drawn through the images and presented in figure 2.

strong regularization was imposed on all voxels, which do not exceed  $M_{\text{bkg}}$  by more than 90% ( $k_2 = 0.9$ ). The 90% value was chosen to include all background regions with noise-related fluctuations up to that threshold. Above that, a much weaker MRP regularization penalty of  $\beta_2 = 0.35$  allows a stronger, but yet controlled, deconvolution in the peak activity regions close to the spheres. Selecting a layer of 3 voxels around the edges ( $R_1 = 3$ ) of the phantom with

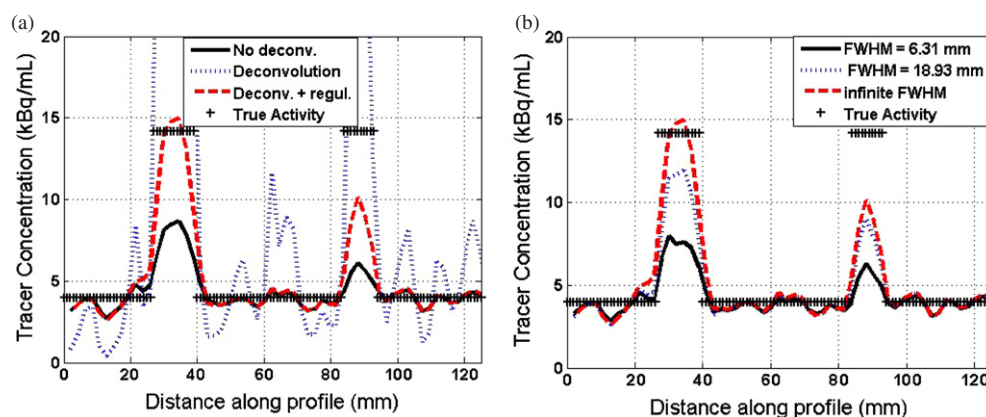


**Figure 2.** (a) Recovered activity concentration profiles across the smallest two spheres of the simulated PET scan (see the arrow in figure 1), before and after deconvolution, and after deconvolution with the described regularization, when a deconvolution function (DF) with infinite full width at half-maximum (FWHM) was used; (b) effect of the FWHM of the DF on the same profile when the same regularization parameters were used. Fourteen iterations were used in all cases. The crosses indicate the true activity levels.

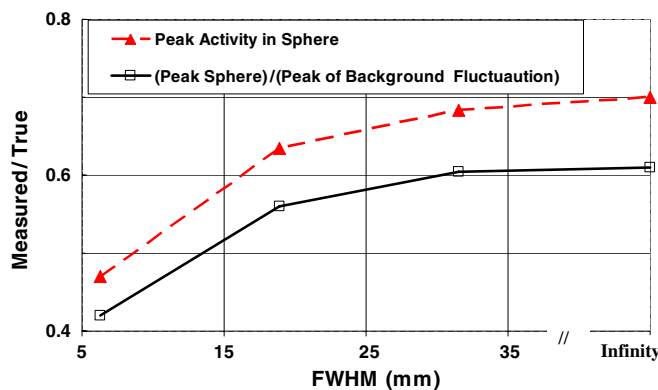


**Figure 3.** Measured over true ratios of the peak activity (triangles) and (peak sphere)/(peak of background fluctuation) (squares) in the smallest, 10 mm diameter sphere, as a function of the FWHM of the deconvolution function. Some of the data points correspond to the profiles displayed in figure 2(b).

even stronger regularization ( $\beta_1 = 1.1$ ) allows us to control the MLEM edge artifacts (Snyder *et al* 1987).

As is illustrated in figures 1, 2(a) and 4, applying such topology-dependent regularization allows the reduction of the variance in background regions and PVE correction improvement in high gradient regions.

### 3.2. Recovery of activity profiles and mean contrast

The recovery of the activity profiles is illustrated in figures 2, 4(a) and (b) for the 10, 13, 22 and 28 mm spheres for the simulated scan and in figure 4(c) for the 10 and 37 mm spheres of the experimental scan.

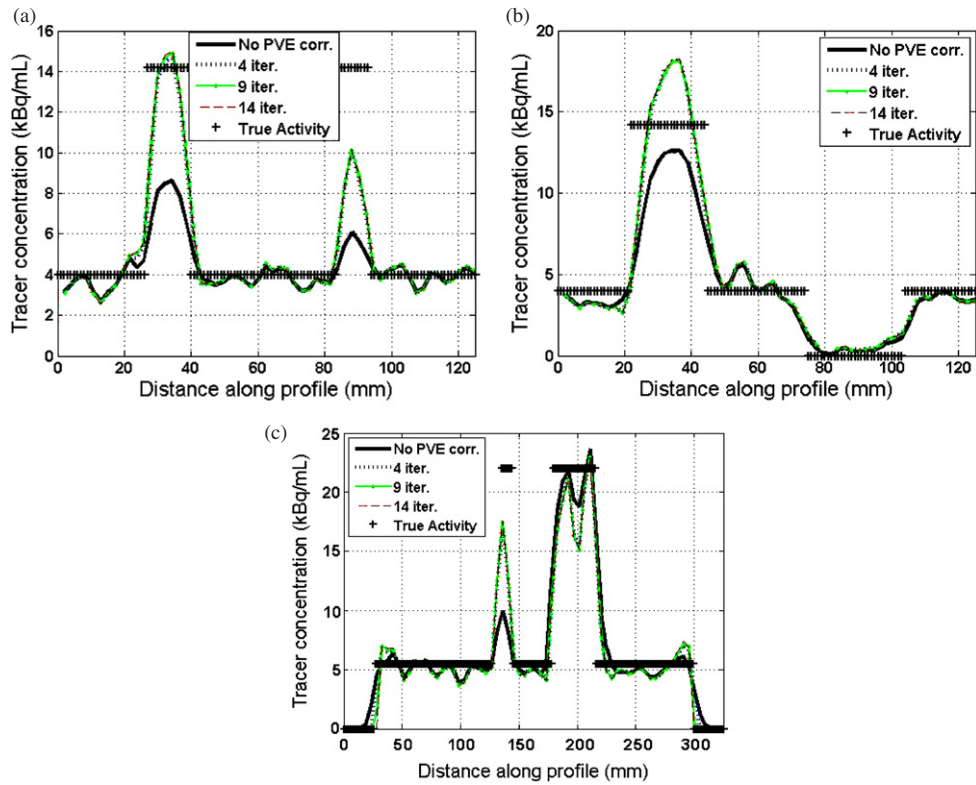


**Figure 4.** Recovery of activity profiles passing through the center of the 13 and 10 mm (a) and the 22 and 28 mm (b) diameter spheres in a simulated scan, and of the 10 and 37 mm spheres in a measured scan (c) of the NEMA image quality phantom (figure 1). The crosses indicate the true activity levels and their approximate location.

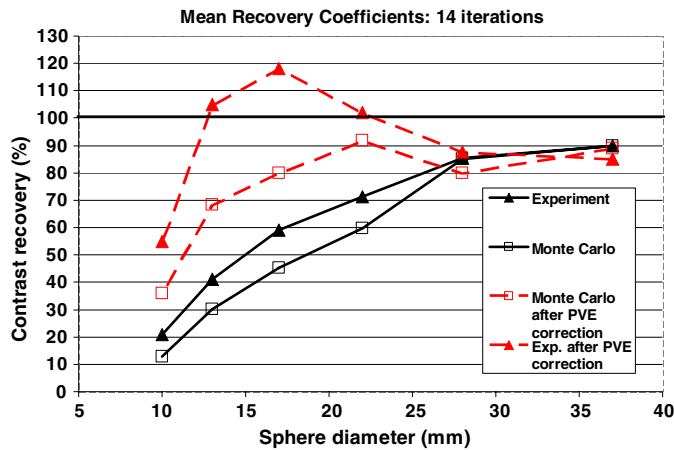


**Figure 5.** Mean contrast recovery before (solid) and after regularized deconvolution (dashes) for the simulated (squares) and experimental scans (triangles) of the NEMA image quality phantom.

The profiles of the spheres after the PVE correction are in general closer to the true activity profiles with the following exceptions: (i) the central profile across some of the spheres may

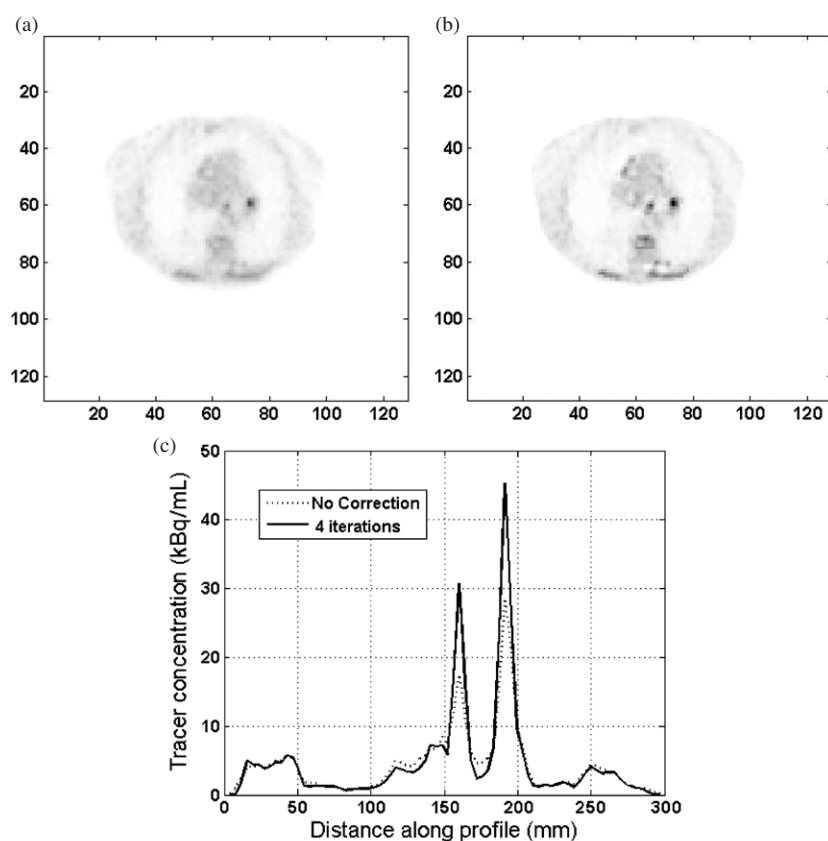


**Figure 6.** Transaxial PET slices of a lung cancer patient before (a) and after PVE correction (b) using the described method. A fixed inverse gray scale was used. Profiles through the two mediastinal potential lesions with and without the correction are shown in (c).

overestimate the true activity (figure 4(b)); (ii) non-uniform uptake inside the larger spheres is amplified by the deconvolution (figure 4(c)). Both of these artifacts are natural consequences of the deconvolution, and if the regularization parameters are not carefully chosen this may lead to a substantial loss of mean contrast recovery accuracy.

In the background regions, due to the stronger regularization imposed in this portion of the image, the activity profile differs very little from the activity profiles prior to the PVE correction. An exception is presented by few voxels around the spheres and inside the largest spheres, in which a moderate increase in the variance is observed. Also a small increase of the edge artifacts occurs at the periphery of the phantom (figure 4(c)). However, these are controlled by the regularization weight,  $\beta_1$ , and are difficult to see in the images (figure 1).

For the spheres with diameters between 10 and 22 mm a significant improvement of the RC is seen (figure 5). For these spheres the RC improves from the pre-correction values of 13% to 60% before to 36% to 92% after PVE correction for the simulated data and from 21% to 71% before to 54% to 118% after the correction for the experimental scan. In both cases, the PVE correction presented in this paper reduces the bias in the RC to less than 20% for all spheres except for the 10 mm diameter sphere in the experiment and the 10 and 13 mm diameter spheres in the simulated data. For the largest spheres with diameters of 28 and 37 mm,

there is no improvement of the mean RC. This is independent of whether they are hot (experiment) or cold (simulation).

### 3.3. Test on a patient PET scan

Although the goal of this paper is to show the proof of concept for the presented PVE correction method using phantom data, we present also a result for a FDG patient PET scan obtained in our clinic on the Discovery LS PET/CT scanner in 2D mode (figure 6). The same parameters as for the phantom case were used except for the background activity,  $M_{\text{bkg}}$ , which was set to roughly approximate the middle of the background signal, 4000 Bq, and the coefficient  $k_2$ , for which a value of 3 was selected due to the stronger background variation and stronger uptake in the potential lesions. At four iterations the algorithm has converged. The corrected image shows enhanced uptake in certain parts of the image. Some of them could be potential lesions. The variance is not increased in the rest of the image.

Performing the correction with different values for these two parameters,  $k_2 = 4$  for  $M_{\text{bkg}} = 4000$  Bq, limits the uptake enhancement to the two mediastinal lesions and the chest wall only. Selecting the background to match the highest background in the vicinity of these lesions ( $M_{\text{bkg}} = 7000$  Bq) and  $k_2 = 2$  results in the enhancement of only the more laterally positioned lesion and the chest wall.

## 4. Discussion

### 4.1. Main features of the method

There are two main features of the post-reconstruction PVE correction method described in this paper, which make it different from previously published methods:

- (i) We changed the shape of the deconvolution function. In addition to a PSF approximating that of the scanner, we tested significantly broader functions with FWHM ranging to infinity. The last one, a step function over a cubic region centered at the voxel being corrected provided the best results.
- (ii) We adapted the regularization procedure to the topology (activity levels and activity variance) of the images, rather than prior ‘anatomic’ information about the sphere size and position.

We have shown (figures 2(b) and 3) that the first feature (i) leads to an improved activity and contrast recovery. This result can be explained in the following way. The factor  $[1 + \varepsilon(\bar{u})]$  (2a) updates the activity estimate in the iteration formula (2) relative to the mean activity for the neighborhood of a voxel, rather than relative to the activity weighted closer to that of voxel  $\vec{u}$ , which would be the case for a sharper DF. This dampens the variance increase in the background. Also using a more uniform DF,  $P(\bar{u}|\vec{r})$ , which multiplies  $[1 + \varepsilon(\bar{u})]$  in (2) reduces the variance in the uniform activity regions by more equally weighted averaging of the inaccuracies (2a) of the previous activity estimate over the selected region. A more uniform DF would also enhance deconvolution for the regions with stronger activity change due to giving more weight to the expected larger inaccuracy in such regions.

The above result is a direct consequence of improving the correctness of the mathematical problem by introducing additional regularization within the iterative sequence (Fedorenko 1994). While one can argue that replacing the scanner PSF with a step function results in the loss of inherent information about the scanner, it turns out that regularization of the problem is more critical. The specifics of the scanner enter in the PVE correction through the truncation

width of the deconvolution function (DF) and through the regularization parameters, which are tailored to the type of PET images being corrected.

The second feature, topology-adapted regularization, is important in oncology where PET tracer uptakes do not necessarily conform to that of the anatomical structures identified with CT or MRI. Tumors may occupy only part of an anatomic structure or may protrude in the tissues between such structures or into neighboring organs.

#### 4.2. Comparison to other methods

For uniform activity spheres, the presented method yields activity and contrast recovery accuracy similar to methods that incorporate the position- and direction-dependent detection system response into the reconstruction (Alessio and Kinahan 2006). However, while these and also other methods (Soret *et al* 2007) use anatomical information to govern the penalty term, the method presented here does not. Higher recovery coefficient accuracy is demonstrated in a method based on the 'regional geometric transfer matrix' (Rousset *et al* 1998) and also with a multiresolution image-based approach acting at a voxel level (Boussion *et al* 2006). Both of these methods use high resolution anatomical images in order to achieve that. Another post-reconstruction PVE correction method (Teo *et al* 2007) also produced higher recovery coefficient accuracy acting at voxel level, but in this paper the problem of variance increase throughout the image was left for future studies.

In the Soret *et al* classification, the PVE correction methods are divided in two groups, which both have disadvantages: (a) correction methods applied at regional level which improve local contrast recovery, but are not suitable for visual image analysis and (b) correction methods applied at voxel level, which rely on the joint use of anatomic information. The method presented here has the potential to resolve these problems: it simultaneously improves local contrast recovery (quantification), provides improved images for visual analysis and does not rely on anatomic information.

According to a recent conference report, such capabilities were shown also for a different approach (Boussion *et al* 2007). The main difference between the two methods is that in the method of Boussion *et al*, the noise suppression is wavelet-based and fully automatic. In our method the user would need to select few regularization parameters based on the properties of the PET images. In that respect, it could be used to selectively enhance the PVE correction for parts of the image with physician-selected levels of activity concentrations and activity concentration variations.

#### 4.3. PVE correction for realistic cases with non-uniform background

The topology adaptive regularization algorithm presented in this paper allows the selective enhancement of deconvolution in the areas of elevated activity and successfully controls variance increases within the rest of the image, without using any prior anatomic information from CT or MRI studies. This was demonstrated also for a patient PET scan containing strong TC non-uniformity and potential mediastinal lung lesions.

For the presented patient image only two parameters are needed to be changed with respect to the phantom cases: the background activity  $M_{\text{bkg}}$  and the factor  $k_2$ , which determines the variation threshold above which the TC would be considered to be above the noise fluctuations. As pointed in section 3.3, the modification of these parameters allows limiting the PVE correction to medically significant parts of the image. Other regularization parameters, e.g. the regularization weight  $\beta_2$ , may also need to be changed for large tumors with non-uniform uptake in order to limit the variance increase within such lesions. We consider it prudent to

leave the selection of the threshold separating noise from significant activity changes to the physician.

We foresee two possible ways of using the described PVE correction method: (1) by user selection of the regularization parameters, which can limit the strength and the threshold for enhancing TC variations to medically relevant regions and limits; (2) by using fixed parameters, previously optimized to give the highest quantification accuracy for PET scans with similar properties. The successful implementation of either of these approaches requires further investigation. For the first approach, a large data base of PET scans will need to be analyzed together with radiologists and radiation oncologists for different tumor sizes, tumor locations and uptake uniformity distributions. For the second approach, an extensive validation of the method using optimized parameters against experimental or numerical phantoms with non-uniform uptake in known lesions needs to be performed.

Special attention to validation will be needed also when the PVE correction is applied to large tumors with heterogeneous uptake or lesions with steep boundaries, since the method will increase the variance for such regions. This is seen in the increased dip in the profile of the large sphere in figure 4(c) and in the small edge artifacts around the spheres in figure 1. No such artifacts are however expected for small lesions due to more gradual uptake increase (figures 6(b) and (c)).

## 5. Conclusion

Introducing a deconvolution function with a step function shape and topology adaptive regularization in maximum-likelihood-based iterative deconvolution lays the basis of a novel approach for controlling image variance. Applying this method to a phantom with uniform activity spheres improved quantification accuracy without increasing the variance in the rest of the image. Testing the method for patient images increased the visibility of small lesions in non-uniform background, while in the same time preserving image quality.

Two ways for clinical implementations are possible: (1) by user selection of the regularization parameters, which can limit the strength and threshold for enhancing activity variations to medically important regions; (2) by using fixed parameters, previously optimized to give highest quantification accuracy for PET scans with similar properties. Both implementations depend on further evaluation and validation with extensive image sets and realistic phantoms with known lesions.

## References

- Alenius S 1999 On noise reduction in iterative image reconstruction algorithms for emission tomography: Median root prior *PhD Thesis* Tampere University of Technology, Tampere, Finland
- Alenius S and Ruotsalainen U 1997 Bayesian image reconstruction for emission tomography based on median root prior *Eur. J. Nucl. Med.* **24** 258–65
- Alessio A M and Kinahan P E 2006 Improved quantitation for PET/CT image reconstruction with system modeling and anatomical priors *Med. Phys.* **33** 4095–103
- Alessio A, Sauer K and Kinahan P 2006 Analytical reconstruction of deconvolved Fourier rebinned PET sinograms *Phys. Med. Biol.* **51** 77–93
- Boussion N, Hatt M, Lamare F, Bizais Y, Turzo A, Cheze-Le-Rest C and Visvikis D 2006 A multiresolution image based approach for correction of partial volume effects in emission tomography *Phys. Med. Biol.* **51** 1857–76
- Boussion N, Hatt M, Reilhac A and Visvikis D 2007 Fully automated partial volume correction in PET based on a wavelet approach without the use of anatomical information *IEEE Nuclear Science Symposium and Medical Imaging Conference Record, Paper M12-5 (Honolulu, HI, USA, October 27–November 3, 2007)*
- Csiszar I 1991 Why least squares and maximum entropy? An axiomatic approach to inference for linear inverse problems *Ann. Stat.* **19** 2032–66

- Fedorenko R P 1994 *Introduction to Computational Physics* (Moscow: Moscow Institute of Physics and Technology Publishers) (in Russian)
- Haber S F, Derenzo S E and Uber D 1990 Application of mathematical removal of positron range blurring in positron emission tomography *IEEE Trans. Nucl. Sci.* **NS-37** 1293–9
- Hoffman E J, Huang S C and Phelps M E 1979 Quantitation in positron emission computed tomography: 1. Effect of object size *J. Comput. Assist. Tomogr.* **3** 299–308
- Hoffman E J, Huang S C, Plummer D and Phelps M E 1982 Quantitation in positron emission computed tomography: 6. Effect of nonuniform resolution *J. Comput. Assist. Tomogr.* **6** 987–99
- Kessler R M, Ellis J R Jr and Eden M 1984 Analysis of emission tomographic scan data: limitations imposed by resolution and background *J. Comput. Assist. Tomogr.* **8** 514–22
- Kirov A S, Piao J Z, Mathur N K, Miller T R, Devic S, Trichter S, Zaider M, Soares C G and Losasso T 2005 The three-dimensional scintillation dosimetry method: test for a (106)Ru eye plaque applicator *Phys. Med. Biol.* **50** 3063–81
- Levin C S and Hoffman E J 1999 Calculation of positron range and its effect on the fundamental limit of positron emission tomography system spatial resolution *Phys. Med. Biol.* **44** 781–99
- Liang Z 1994 Detector response restoration in image reconstruction of high resolution positron emission tomography *IEEE Trans. Med. Imaging* **13** 314–21
- NEMA 2001 *Performance Measurements of Positron Emission Tomographs, NEMA Standards Publication NU 2-2001* (Rosslyn, VA: National Electrical Manufacturers Association)
- Phelps M E, Hoffman E J, Mullani N A and Ter-Pogossian M M 1975 Effect of positron range on spatial resolution *J. Nucl. Med.* **16** 649–52
- Piao Z and Kirov A S 2001 Effect of median root prior (MRP) regularization on the accuracy and convergence of maximum likelihood expectation maximization algorithm applied to 3D scintillation dosimetry (abstract on the AAPM website: <http://www.aapm.org/meetings/01/AM/prabs.asp?mid=6&aid=7358>) 2001 *Annual Meeting of the American Association of Physicists in Medicine* (Salt Lake City, UT)
- Rizzo G, Castiglioni I, Russo G, Tana M G, Dell'Acqua F, Gilardi M C, Fazio F and Cerutti S 2007 Using deconvolution to improve PET spatial resolution in OSEM iterative reconstruction *Methods Inf. Med.* **46** 231–5
- Rousset O G, Ma Y and Evans A C 1998 Correction for partial volume effects in PET: principle and validation *J. Nucl. Med.* **39** 904–11
- Sanchez-Crespo A, Andreo P and Larsson S A 2004 Positron flight in human tissues and its influence on PET image spatial resolution *Eur. J. Nucl. Med. Mol. Imaging* **31** 44–51
- Schmidtlein C R *et al* 2005 Validation of GATE Monte Carlo simulations of the noise equivalent count rate and image quality for the GE Discovery LS PET scanner *Proc. AAPM 47th Annual Meeting (Seattle, WA, July 24–28, 2005) Med. Phys.* **32** 1900–1
- Schmidtlein C R, Kirov A S, Bidaut L, Nehmeh S, Erdi Y, Ganin A, Stearns C W, McDaniel D L, Humm J and Amols H 2006 Validation of GATE Monte Carlo simulations for the GE Advance/Discovery LS PET scanners *Med. Phys.* **33** 198–208
- Snyder D L, Miller M I, Thomas L I Jr and Polite D G 1987 Noise and edge artifacts in maximum-likelihood reconstructions for emission tomography *IEEE Trans. Med. Imaging* **MI-6** 228–38
- Snyder D, Schulz T and O'Sullivan J 1992 Deblurring subject to non-negativity constraints *IEEE Trans. Sig. Proc.* **40** 1143–50
- Soret M, Bacharach S L and Buvat I 2007 Partial-volume effect in PET tumor imaging *J. Nucl. Med.* **48** 932–45
- Teo B K, Seo Y, Bacharach S L, Carrasquillo J A, Libutti S K, Shukla H, Hasegawa B H, Hawkins R A and Franc B L 2007 Partial-volume correction in PET: validation of an iterative postreconstruction method with phantom and patient data *J. Nucl. Med.* **48** 802–10
- Tomic N, Thompson C J and Casey M E 2005 Investigation of the 'Block Effect' on spatial resolution in PET detectors *IEEE Trans. Nucl. Sci.* **52** 599–605
- Turkheimer F E, Bousson N, Anderson A N, Pavese N, Piccini P and Visvikis D 2008 PET image denoising using a synergistic multiresolution analysis of structural (MRI/CT) and functional datasets *J. Nucl. Med.* **49** 657–66
- Wallis J W and Miller T R 1993 Rapidly converging iterative reconstruction algorithms in single-photon emission computed tomography *J. Nucl. Med.* **34** 1793–800